Whole-System Ultrasound Resonances as the Basis for Acoustophoresis in All-Polymer Microfluidic Devices

Rayisa P. Moiseyenko and Henrik Bruus*

Department of Physics, Technical University of Denmark, DTU Physics Building 309, 2800 Kongens Lyngby, Denmark

(Received 14 September 2018; revised manuscript received 19 November 2018; published 8 January 2019)

Using a previously-well-tested numerical model, we demonstrate that good acoustophoresis can be obtained in a microchannel embedded in an acoustically soft, all-polymer chip by excitation of whole-system ultrasound resonances. In contrast to conventional techniques based on a standing bulk acoustic wave inside a liquid-filled microchannel embedded in an elastic, acoustically hard material, such as glass or silicon, the proposed whole-system resonance does not need high acoustic contrast between the liquid and the surrounding solid. Instead, it relies on the very high acoustic contrast between the solid and the surrounding air. In microchannels of usual dimensions, we demonstrate by numerical simulations the existence of whole-system resonances in an all-polymer device that supports acoustophoresis of a quality fully comparable to that of a conventional hard-walled system. Our results open up the possibility of using cheap and easily processable polymers in a controlled manner to design and fabricate microfluidic devices for single-use acoustophoresis.

DOI: 10.1103/PhysRevApplied.11.014014

I. INTRODUCTION

A steadily increasing number of papers report successful applications of ultrasound-based microscale acoustofluidic devices in biology, environmental and forensic sciences, and clinical diagnostics [1–5]. Examples include cell synchronization [6], enrichment of prostate cancer cells in blood [7], high-throughput cytometry and multiple-cell handling [8,9], single-cell patterning and manipulation [10,11], size-independent sorting of cells [12], and rapid sepsis diagnostics by detection of bacteria in blood [13]. Acoustic forces have also been used for noncontact microfluidic trapping and particle enrichment [14], massively parallel force microscopy on biomolecules [15], and acoustic tweezing [16–19].

In all applications, an appropriate magnitude of the acoustic forces is achieved by resonant actuation of ultrasound waves by one of two basic methods. One method relies on bulk acoustic waves (BAWs) [see Fig. 1(a)], for which resonant modes are built up in liquid-filled acoustic resonators, say, microchannels or microcavities, embedded in an acoustically hard material such as silicon, glass, and/or metal. For this method to work, it is crucial that the acoustic contrast between the liquid and the surrounding solid is sufficiently large, typically around 10 in terms of the acoustic impedance ratio. The other method relies on surface acoustic waves (SAWs) [Fig. 1(b)] that are resonantly excited by use of appropriately spaced interdigitated metallic transducer electrodes positioned on the surface of a piezoelectric substrate. For this method to work, it is crucial that the piezoelectric coupling constant of the substrate is sufficiently strong, and thus a popular choice of substrate is lithium niobate, which is well known from conventional electromechanical filters in microwave technology. Both methods are actively being used in contemporary acoustofluidics as is evident from the following examples published in the literature the past 2 years: BAW devices have been used for cell focusing in simple and inexpensive aluminum devices [20], for binary-particle separation in droplet microfluidics [21], for hematocrit determination [22], for enrichment of tumor cells from blood [23], and for manipulation of *Caenorhabditis elegans* [24,25], while SAW devices have been used for nanoparticle separation [26,27], for self-aligned particle focusing and patterning [28], for enhanced cell sorting [29], and for in-droplet microparticle separation [30].

Currently, the acoustofluidic devices with the highest throughput are of the BAW type [5]. However, a limiting factor for fully exploiting the application potential of such devices is the cost of the glass or silicon components used because of their high acoustic contrast relative to water. This limitation is especially severe for applications intended for point-of-care clinical use [3], where the acoustic separation unit must be a single-use consumable. This important problem could be overcome by use of all-polymer microfluidic devices if they could be made compatible with ultrasound acoustics, because that would allow cheap conventional volume fabrication [31].

*bruus@fysik.dtu.dk

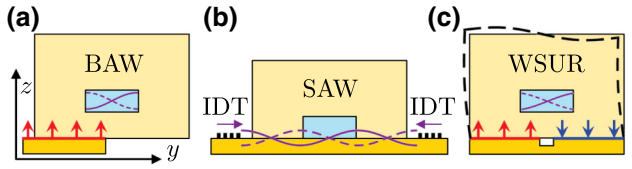

FIG. 1. The conventional and proposed acoustophoresis techniques for a liquid-filled microchannel (blue) embedded in an elastic solid (beige). (a) BAWs exited by a single piezoelectric actuator (orange). (b) SAWs excited by interdigitated transducers (IDT; black) on a piezoelectric substrate (orange). (c) The proposed WSURs excited by two piezoelectric actuators excited in antiphase (red and blue arrows). Magenta and dashed black curves represent pressure and displacement fields, respectively.

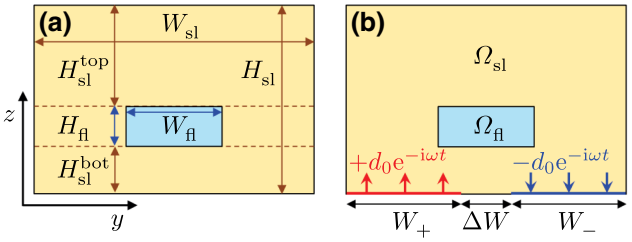

FIG. 2. (a) The vertical cross section in the y-z plane of the long, straight device. The elastic solid (beige, $\Omega_{\rm sl}$) has outer width $W_{\rm sl}$ and height $H_{\rm sl}$, while the fluid channel (light blue, $\Omega_{\rm fl}$) has width $W_{\rm fl} = 377\ \mu$m and height $H_{\rm fl} = 157\ \mu$m. (b) The antisymmetric actuation $\mathbf{u}(W_\pm) = \pm d_0\, e^{-i\omega t}\mathbf{n}$ of the time-harmonic displacement in the actuation regions W_+ (red) and W_- (blue) separated by the gap ΔW.

However, partly due to the lack of good theoretical understanding, it has proven difficult to make good all-polymer BAW devices for acoustofluidics. However, a few results for such devices have been published, including focusing of polymer beads [32–35], lipids [32], and red blood cells [33,36], as well as blood-bacteria separation [37] and purification of lymphocytes [38]. A potential drawback of using polymer-based acoustofluidic devices could be the increased energy dissipation and heating in the polymers during operation. However, for the purpose of this study, we imagine the use of a standard temperature control often used in acoustofluidics, such as a Peltier-element feedback loop [39], and thus omit an analysis of thermal effects.

The main goal of this work is to provide a theoretical framework for the design of all-polymer microfluidic devices capable of successful acoustophoretic applications. The structure of this paper is as follows: In Sec. II, we present the basic device geometry and the material properties. In Sec. III, we give a short overview of the theory of linear acoustics of the solid and the fluid, the acoustic radiation force on suspended tracer microparticles, and the numerical implementation of the model. The results of the numerical simulation for a simplified model in two dimensions of a conventional silicon-glass system are shown and analyzed in Sec. IV. They serve as a baseline for the two-dimensional (2D) simulation results of an all-polymer device presented in Sec. V, where the principle of whole-system ultrasound resonances (WSURs) [see Fig. 1(c)] is established as a method to identify specific resonances suitable for successful acoustophoresis in this acoustically soft system. In Sec. VI, we present the results of a more-realistic model in three dimensions of the all-polymer device, and discuss them in relation to preliminary experimental results. Finally, in Sec. VII, we summarize and discuss the results obtained.

II. GEOMETRY AND MATERIALS

Generic, millimeter-long, straight channels that are placed along the horizontal x axis and have a constant rectangular cross section in the vertical y-z plane have been intensively studied both theoretically [40–43] and experimentally [39,44–46]. This design is thus an obvious choice for our analysis, and following Refs. [39,44–46], the fluid domain $\Omega_{\rm fl}$ in the vertical y-z plane is taken to be a rectangle of width $W_{\rm fl} = 377\ \mu$m and height $H_{\rm fl} = 157\ \mu$m. The fluid domain is embedded in an elastic solid $\Omega_{\rm sl}$ defined by a larger rectangle of width $W_{\rm sl}$ and height $H_{\rm sl}$ (see Fig. 2) with values to be specified later.

As sketched in Fig. 1(c), the ultrasound actuation is modeled by the time-harmonic and spatially antisymmetric displacement condition applied to the bottom surface of the solid with a frequency in the low-megahertz range of 1.0–2.2 MHz and a fixed amplitude $d_0 \simeq 0.1$ nm, which correspond to typical experimental values. This specific actuation is chosen to better generate the conventional antisymmetric standing pressure half-wave in the horizontal direction, which focuses suspended particles in the vertical y-z plane along the center x axis of the channel. The frequency range is where this specific resonance appears for the given choice of geometry and materials. It is straightforward to extend this simple actuation model by adding an actual piezoelectric material to the solid and driving it by a suitable ac voltage.

Materialwise, the elastic solid in our model is taken to be the transparent thermoplastic poly(methyl methacrylate) (PMMA), also known as "acrylic glass" and sold under the trade names Plexiglas and Lucite. The acoustofluidic response of this acoustically soft polymer is contrasted with that of the conventional acoustically hard devices made of a silicon base and a borosilicate glass lid (Pyrex) [39,44–46]. The values of the material parameters at ambient temperature used in the elastodynamic model of the solids are shown in Table I. In the case of PMMA we have used representative average values based on Refs. [47–50,54]. Material parameters at 25 ℃ for water and 10-μ-m-diameter polystyrene tracer particles are listed in Table II.

TABLE I. Material parameters at 25 ℃ for selected solids. The specific acoustic impedance is $Z_{sl} = \sqrt{\rho_{sl} C_{11}}$, and for isotropic materials $C_{12} = C_{11} - 2C_{44}$ (PMMA and Pyrex).

Parameter	Symbol	PMMA	Pyrex	Silicon	Unit
		[47–51]	[52]	[53]	
Mass density	ρ_{sl}	1190	2230	2329	kg/m^3
Elastic modulus	C_{11}	8.567	69.72	165.7	GPa
Elastic modulus	C_{44}	1.429	26.15	79.6	GPa
Elastic modulus	C_{12}	5.710	17.43	63.9	GPa
Damping coefficient	Γ_{sl}	0.0040	0.0004	0	1
Specific impedance	Z_{sl}	3.19	12.47	19.64	MPa s/m

III. THEORY

The physical model of the acoustophoretic device consists of a fluid-filled microchannel channel embedded in an elastic solid. The piezoelectric transducer, which in reality drives the ultrasound waves in the system, is replaced by a simplifying oscillating displacement condition on part of the outer surface of the solid. We thus need the governing equation for the linear ultrasound acoustics of the solid and the fluid, as well as for the nonlinear acoustics describing the acoustophoretic forces on microparticles suspended in the fluid. We restrict our analysis to the time-periodic and isentropic case at ambient temperature, thus disregarding transient behavior [42] and thermal effects [41,57].

A. Linear acoustics of the solid and the fluid

We use standard, weakly damped, linear elastodynamics [58], with the specific coupling to microscale acoustofluidics as formulated by Ley and Bruus [59] for isotropic solids, and its extension to cubic crystals by Dual and Schwarz [60]. The dynamics of the solid of density ρ_{sl} is modeled by the elastic displacement $\mathbf{u}$ and stress $\boldsymbol{\sigma}$, both with a time-harmonic oscillation given by the phase factor $e^{-i\omega t}$, where $\omega = 2\pi f$ is the angular frequency and f is the frequency. Because the governing equations are linear, this temporal phase factor is divided out in the following, leaving only a spatially dependent amplitude for all fields.

TABLE II. Material parameters at 25 ℃ for water and 10-μm-diameter polystyrene tracer particles. Note: $Z_{fl} = \rho_{fl} c_{fl}$.

Parameter	Symbol	Value	Unit
Water			
Mass density [41]	ρ_{fl}	997.05	kg/m^3
Compressibility, isentropic [41]	κ_{fl}	447.7	TPa^{-1}
Speed of sound [41]	c_{fl}	1496.7	m/s
Damping coefficient [55]	Γ_{fl}	0.004	1
Specific acoustic impedance	Z_{fl}	1.49	MPa s/m
Polystyrene particles in water			
Mass density [56,57]	ρ_{ps}	1050	kg/m^3
Compressibility [56,57]	κ_{ps}	238	TPa^{-1}
Monopole coefficient [57]	f_0	0.468	1
Dipole coefficient [57]	f_1	0.034	1

When time dependence is needed, the phase factor $e^{-i\omega t}$ is simply reintroduced in the fields. The linear constitutive stress-strain relation is given in terms of the elastic moduli C_{ik} in the Voigt representation, and the governing equation for the displacement field $\mathbf{u}$ at angular frequency ω becomes

$$-\rho_{sl}\omega^2 (1 + i\Gamma_{sl})\ \mathbf{u} = \boldsymbol{\nabla}\cdot\boldsymbol{\sigma}, \tag{1a}$$

with

$$\begin{pmatrix}\sigma_{xx}\\ \sigma_{yy}\\ \sigma_{zz}\\ \sigma_{yz}\\ \sigma_{xz}\\ \sigma_{xy}\end{pmatrix} = \begin{pmatrix}C_{11} & C_{12} & C_{12} & 0 & 0 & 0\\ C_{12} & C_{11} & C_{12} & 0 & 0 & 0\\ C_{12} & C_{12} & C_{11} & 0 & 0 & 0\\ 0 & 0 & 0 & C_{44} & 0 & 0\\ 0 & 0 & 0 & 0 & C_{44} & 0\\ 0 & 0 & 0 & 0 & 0 & C_{44}\end{pmatrix}\begin{pmatrix}\partial_x u_x\\ \partial_y u_y\\ \partial_z u_z\\ \partial_y u_z + \partial_z u_y\\ \partial_x u_z + \partial_z u_x\\ \partial_x u_y + \partial_y u_x\end{pmatrix}. \tag{1b}$$

A cubic crystal has three independent elastic moduli C_{11}, C_{12}, and C_{44}, while an isotropic material has two due to the constraint $C_{12} = C_{11} - 2C_{44}$. In the latter case, the material is therefore characterized by the longitudinal and transverse sound speeds $c_{lo} = \sqrt{C_{11}/\rho_{sl}}$ and $c_{tr} = \sqrt{C_{44}/\rho_{sl}}$, respectively.

As described in Ref. [55], the damping of the acoustic wave is taken into account in Eq. (1a) by the factor $1 + i\Gamma_{sl}$. This description is valid for the wide range of solids that all have a small damping coefficient $\Gamma_{sl} = 2\alpha/k_0 < 1$, where α is the attenuation coefficient (measured in nepers per meter) and k_0 is the wavenumber. Here we study the acoustically hard materials silicon and Pyrex with $\Gamma_{si} = 0$ and $\Gamma_{Py} = 0.0004$, respectively [55], and the acoustically soft polymer PMMA with $\Gamma_{PMMA} = 0.0088$ [51]. In the concluding discussion in Sec. VII, we also briefly describe a device made of the rubber polydimethylsiloxane (PDMS).

The acoustic energy density E_{ac}^{sl} in the solid domain is the sum of the kinetic and elastic energy densities:

$$E_{ac}^{sl} = \frac{1}{2}\rho_{sl}\omega^2\langle u_k u_k\rangle + \frac{1}{2}\langle\epsilon_{ik}\sigma_{ik}\rangle, \tag{2}$$

with summation over the repeated indices $i,k = x,y,z$, and where $\epsilon_{ik} = \frac{1}{2}(\partial_i u_k + \partial_k u_i)$ is the strain-tensor components, while $\langle AB\rangle = \frac{1}{2}\mathrm{Re}(A^*B)$ is the time average over one oscillation period of the fields A and B given in the complex time-harmonic notation.

The fluid (water) of density ρ_{fl} and sound speed c_{fl}, with acoustic pressure p and acoustic velocity $\mathbf{v}$ at angular frequency ω, is modeled as pressure acoustics with a weak absorption $\Gamma_{\mathrm{fl}} \ll 1$ but no viscosity [59]:

$$\nabla^2 p = -\frac{\omega^2}{{c_{\mathrm{fl}}}^2}(1 + i\Gamma_{\mathrm{fl}})\, p, \tag{3a}$$

$$\mathbf{v} = \frac{-i}{\omega\rho_{\mathrm{fl}}}\,\nabla p. \tag{3b}$$

The acoustic energy density $E_{\mathrm{ac}}^{\mathrm{fl}}$ in the fluid domain is the sum of the kinetic and compressional energy densities:

$$E_{\mathrm{ac}}^{\mathrm{fl}} = \frac{1}{2}\rho_{\mathrm{fl}}\langle v_k v_k\rangle + \frac{1}{2}\kappa_{\mathrm{fl}}\langle p^2\rangle, \tag{4}$$

where $\kappa_{\mathrm{fl}} = (\rho_{\mathrm{fl}} c_{\mathrm{fl}}^2)^{-1}$ is the compressibility of the fluid.

B. Boundary conditions and fluid-solid coupling

The applied boundary conditions are the usual ones [59]; namely, that (1) the stress and the velocity fields are continuous across all fluid-solid interfaces, which then provides the coupling between the fluid and solid domains, (2) the stress is zero on all outer boundaries facing the air, and (3) the piezoelectric actuation is represented by a given displacement in the normal direction at that part of the solid surface where the actuator is attached. The influence ($\leftarrow$) from the surroundings on a given domain with an outward-pointing surface normal $\mathbf{n}$ is as follows:

$$\text{fluid domain} \leftarrow \text{solid:} \qquad \mathbf{v}\cdot\mathbf{n} = -i\omega\,\mathbf{u}\cdot\mathbf{n}; \tag{5a}$$

$$\text{solid domain} \leftarrow \text{fluid:} \qquad \boldsymbol{\sigma}_{\mathrm{sl}}\cdot\mathbf{n} = -p\,\mathbf{n}; \tag{5b}$$

$$\text{solid domain} \leftarrow \text{transducer:} \qquad \mathbf{u} = \pm d_0\,\mathbf{n}; \tag{5c}$$

$$\text{solid domain} \leftarrow \text{air:} \qquad \boldsymbol{\sigma}_{\mathrm{sl}}\cdot\mathbf{n} = \mathbf{0}. \tag{5d}$$

C. The acoustic radiation force on suspended microparticles

In a good acoustofluidic device, the acoustic radiation force $\mathbf{F}^{\mathrm{rad}}$ on a suspended microparticle should be sufficiently large. In this work we consider 10-μm-diameter spherical polystyrene Styron 666 particles with density ρ_{ps} and compressibility κ_{ps}. For such a large microparticle suspended in water of density ρ_{fl} and compressibility κ_{fl}, thermoviscous boundary layers can be ignored, and the monopole and dipole acoustic scattering coefficients f_0 and f_1 are given by [57]

$$f_0 = 1 - \frac{\kappa_{\mathrm{ps}}}{\kappa_{\mathrm{fl}}} = 0.468, \quad f_1 = \frac{2(\rho_{\mathrm{ps}} - \rho_{\mathrm{fl}})}{2\rho_{\mathrm{ps}} + \rho_{\mathrm{fl}}} = 0.034. \tag{6}$$

In the presence of an acoustic field (3) of pressure p and velocity $\mathbf{v}$, the suspended microparticle experiences an acoustic radiation force $\mathbf{F}^{\mathrm{rad}}$ given by [61]

$$\mathbf{F}^{\mathrm{rad}} = -\pi a^3\left[\frac{2}{3}\,\kappa_{\mathrm{fl}}\mathrm{Re}\big(f_0^*\,p^*\nabla p\big) - \rho_{\mathrm{fl}}\mathrm{Re}\big(f_1^*\,\mathbf{v}^*\cdot\nabla\mathbf{v}\big)\right], \tag{7}$$

where a is the particle radius and the asterisk denotes complex conjugation.

D. Numerical implementation

Following the procedure described in Ref. [59], including mesh convergence tests, the coupled field equations (1) and (3) for the fluid pressure p and the elastic-solid displacement $\mathbf{u}$, subject to the boundary conditions (5), are implemented and solved in weak form with the finite-element solver COMSOL MULTIPHYSICS 5.3a [62]. Lastly, to evaluate the quality of the acoustophoresis in the given device, the last step is to use Eqs. (6) and (7) to compute the acoustic scattering coefficients f_0 and f_1 as well as the acoustic radiation force $\mathbf{F}^{\mathrm{rad}}$ acting on a single 10-μm-diameter spherical polystyrene tracer bead suspended at different positions in the water-filled microchannel.

IV. RESULTS FOR THE 2D MODEL OF A CONVENTIONAL HARD-WALLED DEVICE

We begin our analysis with the computationally-less-demanding and faster simulations restricted to 2D cross sections of the systems before moving on to the more-computationally-demanding, full three-dimensional (3D) simulations. Moreover, to establish a baseline for evaluating the results for the acoustophoretic capabilities of all-polymer devices, we first analyze an ideal hard-walled device. Then we progress to a conventional, acoustically hard but elastic silicon-glass device before finally treating an all-polymer device. In the main part of the paper, we analyze the standing half-wave pressure resonance along the y direction, but as shown in Sec. VII, the analysis can straightforwardly be extended to higher modes with a more-complex spatial structure.

A. An ideal hard-walled device in two dimensions

We consider a rectangular channel cross section of width W_{fl} and height H_{fl} in the vertical y-z plane and centered around $y = 0$. If its walls are infinitely hard, it supports

TABLE III. The length scales of the rectangular silicon-Pyrex system with a fluid-filled rectangular channel. The values are from Ref. [44], except for ΔW, which is introduced in Fig. 2(b).

Dimension	Solid domain	Fluid domain
Length	$L_{sl} = 50$ mm	$L_{fl} = 40$ mm
Width	$W_{sl} = 2.52$ mm	$W_{fl} = 377\ \mu$m
Height	$H_{si} = 350\ \mu$m	$H_{fl} = 157\ \mu$m
Height	$H_{Py} = 1130\ \mu$m	⋯
Actuator gap	$\Delta W = 100\ \mu$m	⋯

a standing half-wave pressure resonance p_{hard} in the horizontal y direction at the frequency f_{hard}. The resonance is characterized by its amplitude p_{ac} and corresponding acoustic energy density E_{hard}, and it results in a radiation force $\mathbf{F}^{rad}_{hard}$ of amplitude F^{rad}_{ac} on a given spherical tracer particle of radius a and acoustic monopole and dipole scattering coefficients f_0 and f_1 suspended in the channel. With use of the dimensions of the fluid domain listed in Table III, the resonance properties can be summarized as [45]

$$f_{hard} = \frac{c_{fl}}{2W_{fl}} = 1.985\ \text{MHz}, \tag{8a}$$

$$p_{hard} = p_{ac} \sin k_y y, \quad \text{with } k_y = \frac{\pi}{W_{fl}}, \tag{8b}$$

$$E_{hard} = \frac{1}{4}\kappa_{fl} p_{ac}^2, \tag{8c}$$

$$\mathbf{F}^{rad}_{hard} = -F^{rad}_{ac} \sin\left(2k_y y\right) \mathbf{e}_y, \quad \text{with } F^{rad}_{ac} = \left(\frac{f_0}{3} + \frac{f_1}{2}\right) 4\pi^2 \frac{a^3 E_{hard}}{W_{fl}}. \tag{8d}$$

This hard-walled resonance is completely decoupled from the motion of the surrounding solid. Its standing pressure wave p_{hard} is a perfect sinusoidal half-wave with a vertical nodal line at the channel center, and the radiation force $\mathbf{F}^{rad}_{hard}$ is similarly a perfect sinusoidal full-wave that pushes suspended particles horizontally toward their stable equilibrium positions at the vertical center plane of the channel. No vertical force is exerted.

The f_{hard} resonance is an idealization of the standing pressure half-wave used in many acoustophoresis experiments. In the following study, we choose this resonance as the prime example of an acoustic resonance that leads to particularly good acoustophoresis.

B. A conventional silicon-glass device in two dimensions

As mentioned in Sec. I, silicon-glass devices have successfully been applied to microscale acoustofluidic tasks [6–9,12,13]. Following the experiments reported in Refs. [39,44–46], we choose here to study a long, straight rectangular channel of length L_{fl}, width W_{fl}, and height H_{fl} fabricated by KOH etch into the surface of a rectangular $\langle 100 \rangle$ silicon wafer with length L_{sl}, width W_{sl}, and height $H_{si} = H^{bot}_{sl} + H_{fl}$ that is sealed off with a borosilicate glass lid (Pyrex) of height $H_{Py} = H^{top}_{sl}$ and the same length L_{sl} and width W_{sl}. In the following, we restrict our modeling to the 2D vertical cross section in the y-z plane sketched in Fig. 2(a) using the device dimensions listed in Table III and the antisymmetric actuation of amplitude $d_0 = 0.1$ nm on the bottom surface as sketched in Fig. 2(b) and given in Eq. (5c). The amplitude of d_0 is chosen to result in acoustic energy densities E^{fl}_{ac} and pressure amplitudes p_{ac} in the water matching those experimentally observed. In the literature, the typical range of E^{fl}_{ac} is approximately 1–100 J/m^3 and that of p_{ac} is approximately 0.1–1 MPa [12,33,39,44,46]; it is worth mentioning that despite the large value of the pressure, no acoustic cavitation is observed in the low-megahertz frequency range. Cavitation is therefore left out of the current analysis both for the hard glass-silicon and soft polymer acoustofluidic devices.

Most of the theoretical analysis of the acoustofluidic properties of this microchannel was performed under the assumption of infinitely hard walls [40–42]. This assumption is justified for silicon-glass devices, as these solids are heavier and stiffer than water, as quantified by the ratio Z_{sl}/Z_{fl} of the specific acoustic impedances listed in Tables I and II:

$$\frac{Z^{Py}_{sl}}{Z^{wa}_{fl}} = 8.35, \quad \frac{Z^{si}_{sl}}{Z^{wa}_{fl}} = 13.16. \tag{9}$$

However, as in Ref. [43], we now include the elastic properties of the surrounding elastic silicon and Pyrex material using the parameter values listed in Table I.

According to Eq. (8a), the hard-walled device has a well-defined half-wave resonance at $f_{hard} = 1.985$ MHz. We therefore simulate the silicon-glass device in the frequency range from 1.7 to 2.1 MHz (see Fig. 3). We compute the frequency dependency of the acoustic energy in the solid domain $\mathcal{E}^{sl}_{ac}$ and the fluid domain $\mathcal{E}^{fl}_{ac}$, defined by

$$\mathcal{E}^{sl}_{ac} = \int_{\Omega_{sl}} E^{sl}_{ac}\, dydz, \qquad \mathcal{E}^{fl}_{ac} = \int_{\Omega_{fl}} E^{fl}_{ac}\, dydz, \tag{10}$$

as well as the frequency dependency of the spatial average $\bar{\mathbf{F}}^{rad}$ of the acoustic radiation force on a 10-μm-diameter test particle in the fluid domain:

$$\bar{F}^{rad}_y = \frac{1}{W_{fl}H_{fl}} \int_{\Omega_{fl}} \frac{y}{|y|} F^{rad}{}_y\, dydz, \tag{11a}$$

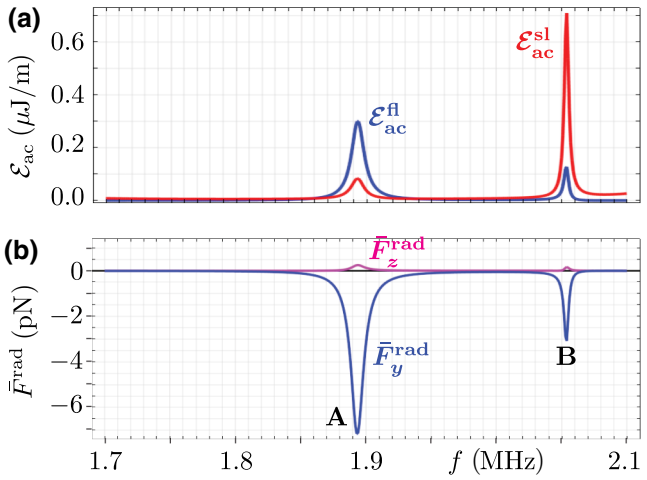

FIG. 3. Numerical results for the frequency dependency of the rectangular silicon-glass device actuated at frequency f with the antisymmetric actuation in Fig. 2(b) with displacement amplitude $d_0 = 0.1$ nm. Two strong resonances A and B are identified. (a) Line plot of the total acoustic energy $\mathcal{E}^{fl}_{ac}$ (blue) in the fluid domain Ω_{fl} and the total acoustic energy $\mathcal{E}^{sl}_{ac}$ (red) in the solid domain Ω_{sl} versus f for the silicon-glass device. (b) The spatially averaged radiation-force components $\bar{F}^{rad}_y$ (blue) and $\bar{F}^{rad}_z$ (magenta).

$$\bar{F}^{rad}_z = \frac{1}{W_{fl}H_{fl}} \int_{\Omega_{fl}} \left|F^{rad}_z\right| dydz. \tag{11b}$$

Here we have "rectified" the y-component average through the antisymmetric prefactor $y/|y|$ to obtain a large value of $\bar{F}^{rad}_y$ when F^{rad}_y has the useful antisymmetric form and where we have taken the absolute value of F^{rad}_z before averaging so that a minimal value of $\bar{F}^{rad}_z$ is obtained when the magnitude of the vertical component of the acoustic radiation force is small everywhere. This is done to help identify resonances having a behavior similar to the conventional and very useful behavior of the hard-walled device; see Eq. (8).

The results for $\mathcal{E}^{sl}_{ac}$, $\mathcal{E}^{sl}_{ac}$, $\bar{F}^{rad}_y$, and $\bar{F}^{rad}_z$ versus frequency are shown in Fig. 3. We readily identify two strong resonances A and B that show up in all four quantities at $f_A = 1.893$ MHz and $f_B = 2.054$ MHz, respectively. Acoustically, these resonances are different. In Fig. 3(a) we see that for resonance A, the acoustic energy $\mathcal{E}^{fl}_{ac} = 0.300$ J/m in the fluid is 3.7 times larger than $\mathcal{E}^{sl}_{ac} = 0.082$ J/m in the solid, in spite of the area $\mathcal{A}_{fl} = 0.059$ mm^2 of the fluid domain being 62 times smaller than the area $\mathcal{A}_{sl} = 3.670$ mm^2 of the solid domain. Thus, resonance A may be characterized as a fluid-domain resonance. Conversely, for resonance B, $\mathcal{E}^{fl}_{ac} = 0.127$ J/m in the fluid is 0.18 times $\mathcal{E}^{sl}_{ac} = 0.710$ J/m in the solid, and resonance B may thus be characterized as a whole-system resonance.

This characterization is corroborated by our studying the Q factors of the resonances, defined for resonance A as $Q_A = f_A/\Delta f_A = 161$, where Δf_A is the full width at half maximum of the resonance curve $\mathcal{E}^{fl}_{ac,A}(f)$ in Fig. 3(a), and similarly for resonance B, $Q_B = 501$, both values in agreement with experiment [44]. Following the Q-factor analysis in Ref. [55], we explain the observed Q factors in terms of the respective Q factors $Q_{fl} = 1/2\Gamma_{fl} = 125$ and $Q_{sl} = 1/2\Gamma_{sl} = 1250$ for the fluid domain and the solid domain, respectively. As the damping in a given domain is proportional to the stored energy, the resulting damping coefficient of a resonance is the weighted average of the domain damping coefficients. We can thus estimate the resulting Q factors of resonances A and B as

$$Q^{est}_A = \frac{1}{2}\frac{1}{\Gamma_A} = \frac{1}{2}\frac{\mathcal{E}^{fl}_{ac,A} + \mathcal{E}^{sl}_{ac,A}}{\mathcal{E}^{fl}_{ac,A}\Gamma_{fl} + \mathcal{E}^{sl}_{ac,A}\Gamma_{sl}} = 156, \tag{12a}$$

$$Q^{est}_B = \frac{1}{2}\frac{1}{\Gamma_B} = \frac{1}{2}\frac{\mathcal{E}^{fl}_{ac,B} + \mathcal{E}^{sl}_{ac,B}}{\mathcal{E}^{fl}_{ac,B}\Gamma_B + \mathcal{E}^{fl}_{ac,B}\Gamma_B} = 528. \tag{12b}$$

These estimates deviate by only 5% from the numerical values for Q_A and Q_B listed in Table IV, and we see that Q_A is smaller than Q_B because for resonance A a larger fraction of the damping occurs in the fluid, which has the higher damping, while the opposite is true for resonance B.

In Fig. 3(b) we observe that for both resonance A and resonance B the magnitude $\bar{F}^{rad}_y$ of the horizontal component of $\bar{\mathbf{F}}^{rad}$ is much larger than that of the vertical component $\bar{F}^{rad}_z$. To quantify this observation, we introduce the figure of merit R, listed in Table IV, as the ratio

$$R = -\frac{\bar{F}^{rad}_y}{\bar{F}^{rad}_z}. \tag{13}$$

R will be large in situations where the acoustic radiation force has the desired property of a large antisymmetric horizontal component and small vertical component. For resonance A R is 29.1 and for resonance B it is 18.1, indicating that the fluid-domain resonance A has better acoustophoretic properties than the whole-system resonance B. We also note that the predicted acoustic energy densities E_{ac} at the two resonances listed in Table IV,

TABLE IV. The Q factor, the fluid-domain-averaged acoustic energy density E^{fl}_{ac}, the components of the average acoustic radiation force $\bar{\mathbf{F}}^{rad}$, and the figure of merit R for resonances A and B in Fig. 3 in the silicon-glass device of width $W_{sl} = 2.52$ mm and height $H_{sl} = 1.48$ mm for $d_0 = 0.1$ nm.

Resonance	Frequency (MHz)	Q	E^{fl}_{ac} (Pa)	$\bar{F}^{rad}_y$ (pN)	$\bar{F}^{rad}_z$ (pN)	R
A	1.893	161	5.07	7.15	0.25	29.1
B	2.054	501	2.15	3.08	0.17	18.1

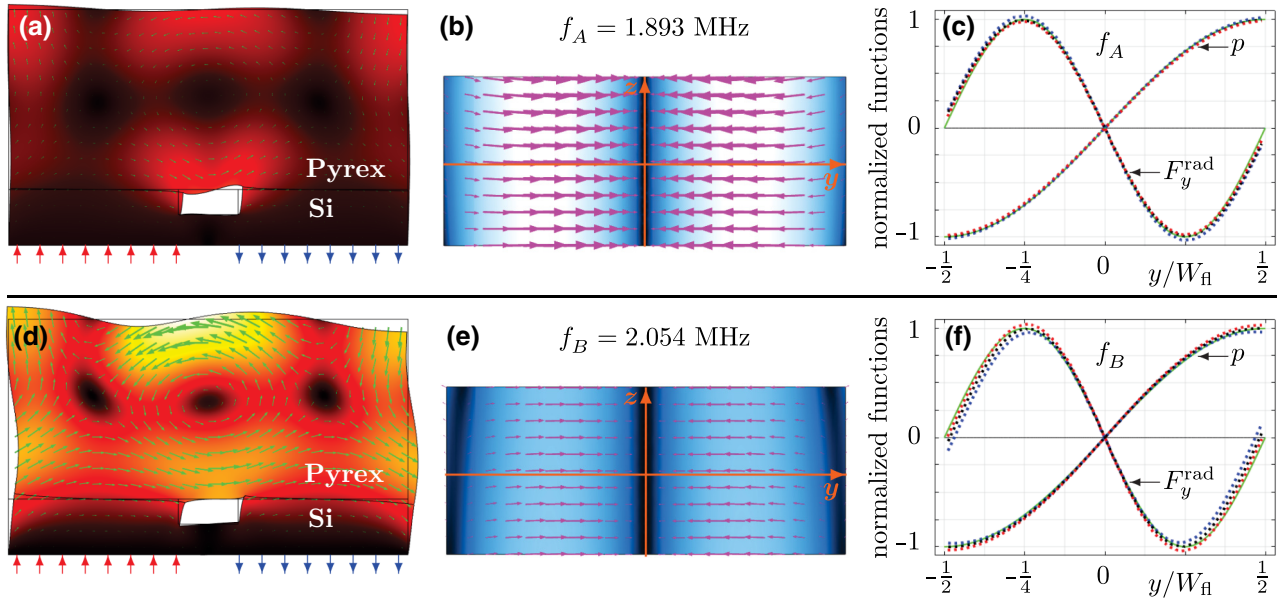

FIG. 4. Numerical results for resonances A and B in Fig. 3 of the glass-silicon device. (a)–(c) are for $f_A = 1.893$ MHz. (a) Vector plot in the solid domain $\Omega_{\rm sl}$ of the displacement field $\mathbf{u}$ (green arrows) and color plot of its amplitude u from 0 nm (black) to 2.6 nm (white). To be visible, the nanometer-scale displacement has been increased by a factor of 50 000. (b) The radiation force $\mathbf{F}^{\rm rad}$ on a 10-μm-diameter spherical polystyrene tracer particle as a function of its position in the fluid domain $\Omega_{\rm fl}$. Color plot of the magnitude $F^{\rm rad}$ from 0 pN (black) to 11.5 pN (white) and vector plot (magenta arrows) of $\mathbf{F}^{\rm rad}$. (c) Comparison of the numerical simulation of the silicon-glass device (dotted lines) in Fig. 3 with the analytical result for the hard-wall device (solid green line). The normalized pressure $p/p_{\rm norm}$ (half-wave, $p_{\rm norm} = 209$ kPa) and y component of the radiation force $F_y^{\rm rad}/F_{\rm norm}^{\rm rad}$ (full wave, $F_{\rm norm}^{\rm rad} = 11.0$ pN) plotted along the top, center, and bottom horizontal lines at $z = 0.9H_{\rm fl}$ (blue dots), $z = 0.5H_{\rm fl}$ (black dots), and $z = 0.1H_{\rm fl}$ (red dots), respectively. (d),(e),(f) are as (a),(b),(c), respectively, but for $f_B = 2.054$ MHz with $p_{\rm norm} = 138$ kPa and $F_{\rm norm}^{\rm rad} = 5.05$ pN.

resulting from the actuation amplitude $d_0 = 0.1$ nm chosen, are in agreement with typical experimental values that fall in the range from 1 to 100 Pa [39,44–46].

We study resonances A and B in more detail in Fig. 4. The color and vector plots in Figs. 4(a) and 4(d) reveal that the displacement $\mathbf{u}$ for resonance A is much larger at the interface with the channel than at the outer surface, while for resonance B the opposite is true. The color and vector plots of the acoustic radiation force $\mathbf{F}^{\rm rad}$ for resonance A in Fig. 4(b) shows that it is nearly identical to the perfectly horizontal radiation force $\mathbf{F}_{\rm hard}^{\rm rad}$ in Eq. (8c) of the hard-walled device with its vertical line of stability in the center of the channel. As seen in Fig. 4(e), resonance B is weaker but is quite similar except for some skewness at the sides. Finally, through the horizontal line plots of the radiation force $F^{\rm rad}{}_y$ and the pressure p at the top, center, and bottom heights $z = 0.9H_{\rm fl}$, $0.5H_{\rm fl}$, and $0.1H_{\rm fl}$ shown in Figs. 4(c) and 4(f), we compare more closely resonance f_A and f_B in the silicon-glass device with the ideal half-wave resonance $f_{\rm hard}$ in the hard-walled device. It is seen how closely the pressure p and the y-component of the radiation force $F_y^{\rm rad}$ at the resonance f_A reproduce the corresponding analytical expressions (8b) and (8c) of the resonance $f_{\rm hard}$. Resonance f_B deviates a little more from resonance $f_{\rm hard}$.

In conclusion, Figs. 3 and 4 demonstrate that in an acoustically hard silicon-glass device, two types of resonances may exist. One type is the fluid-domain resonance, represented by resonance A, defined by high acoustic energy in the fluid domain and relatively little coupling to the solid domain. Compared with the actuation displacement d_0, the amplitude u of the displacement field is relatively large at the inner fluid-solid interface and small at the outer surface of the solid. The resulting acoustic fields and radiation force closely resemble those of the ideal hard-walled case. Conversely, the other type is the whole-system resonance, represented by resonance B, defined by high acoustic energy in the solid domain and low acoustic energy in the fluid domain. The displacement at the outer surface of the solid is larger than at the inner fluid-solid interface. The resulting acoustic fields and radiation force deviate a little from those of the ideal hard-walled case.

V. RESULTS FOR THE 2D MODEL OF AN ALL-POLYMER PMMA DEVICE

We now apply our model to the study of an acoustically soft PMMA device. We expect to see a different behavior compared with the acoustically hard silicon-glass device

because of the small ratio $Z_{\rm sl}/Z_{\rm fl}$ of the specific acoustic impedances listed in Tables I and II:

$$\frac{Z_{\rm sl}^{\rm PMMA}}{Z_{\rm fl}^{\rm wa}} = 2.14, \tag{14}$$

which is 4–7 times smaller than for Pyrex and silicon given in Eq. (9). In particular, we expect the fluid-domain resonances of type A to vanish in this case, leaving only WSURs of type B.

A. Analysis of the 3-mm-wide PMMA device

To investigate this hypothesis, we perform numerical simulations on a PMMA device with the dimensions listed in Table V. These values refer to the preliminary experimental work performed by Pelle Ohlsson and Ola Jakobsson at AcouSort AB in Lund, Sweden, on acoustophoresis in all-polymer devices [63]. The device is fabricated from a thin bottom-layer PMMA film of height $H_{\rm sl}^{\rm bot}$ and width $W_{\rm sl}$ [see Fig. 2(a)], onto which is bonded a thick PMMA block of height $H_{\rm sl}^{\rm top} + H_{\rm fl}$ and the same width $W_{\rm sl}$ that contains a rectangular channel of height $H_{\rm fl}$ and width $W_{\rm fl}$ embossed or milled into its bottom surface. In the model we again use the antisymmetric actuation in Fig. 2(b), typically in the range from 1 to 2.1 MHz but now with the larger actuation displacement amplitude $d_0 = 0.3$ nm to mimic the softer material.

The results for $\mathcal{E}_{\rm ac}^{\rm sl}$, $\mathcal{E}_{\rm ac}^{\rm sl}$, $\bar{F}_y^{\rm rad}$, and $\bar{F}_z^{\rm rad}$ versus frequency in the PMMA device are shown in Fig. 5. We immediately notice one striking difference between these spectra and the spectra for the silicon-glass device in Fig. 3. All the observed resonances are whole-system resonances of type B. The energy $\mathcal{E}_{\rm ac}^{\rm sl}$ of the solid is 1–2 orders of magnitude larger than the energy $\mathcal{E}_{\rm ac}^{\rm fl}$ of the fluid domain. In Fig. 5(a) we need to use a logarithmic scale to be able to see these two energies in the same plot. In Fig. 5(b) we plot the components of the average acoustic radiation force $\bar{F}_y^{\rm rad}$ and $\bar{F}_z^{\rm rad}$, and as before observe that a number of resonances are clearly identified in all four quantities. The six most-prominent resonances and their figure of merit R are listed in Table VI. All the Q factors lie in the narrow range from 116 to 147, comparable to conventional devices, and indeed, because $\Gamma_{\rm fl} = \Gamma_{\rm sl}$ in the water-PMMA device, we expect that $Q \simeq Q_{\rm fl} = Q_{\rm sl} = 125$. The simulated values

TABLE V. The length scales of the rectangular PMMA system with a fluid-filled rectangular channel. The values are provided by AcouSort [63].

Dimension	Solid domain	Fluid domain
Length	$L_{\rm sl} = 50$ mm	$L_{\rm fl} = 40$ mm
Width	$W_{\rm sl} = 3.0$ mm	$W_{\rm fl} = 375\ \mu$m
Height	$H_{\rm sl}^{\rm bot} = 175\ \mu$m	$H_{\rm fl} = 150\ \mu$m
Height	$H_{\rm sl}^{\rm top} + H_{\rm fl} = 1000\ \mu$m	⋯
Actuator gap	$\Delta W = 100\ \mu$m	⋯

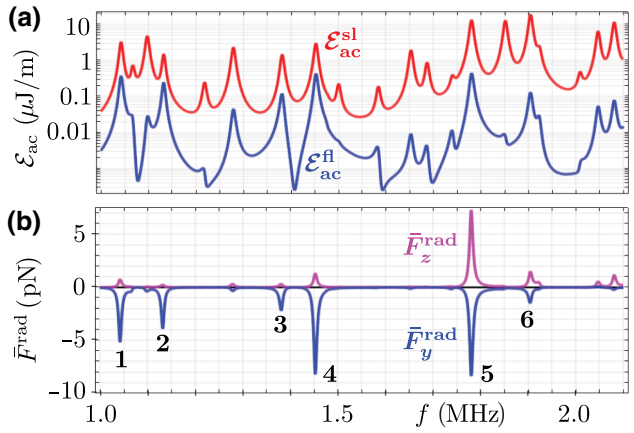

FIG. 5. Numerical results for the rectangular PMMA device actuated at frequency f with the antisymmetric actuation in Fig. 2(b) with displacement amplitude $d_0 = 0.3$ nm. (a) Log-linear plot of the total acoustic energy $\mathcal{E}_{\rm ac}^{\rm fl}$ (blue) in the fluid domain $\Omega_{\rm fl}$ and the total acoustic energy $\mathcal{E}_{\rm ac}^{\rm sl}$ (red) in the solid domain $\Omega_{\rm sl}$ versus actuation frequency f. (b) The spatially averaged radiation-force components $\bar{F}_y^{\rm rad}$ (blue) and $\bar{F}_z^{\rm rad}$ (magenta) as a function of the actuation frequency f showing six prominent resonances, 1–6, also listed in Table VI.

deviate by only 15% from this simple estimate. Further, on the basis of the data in Table VI, we predict that resonance 2 at $f_2 = 1.1320$ MHz with the highest figure of merit, $R_2 = 14.9$, has properties most resembling those of the ideal resonance $f_{\rm hard}$, while resonance 6 at $f_6 = 1.9045$ MHz, the one closets to the ideal resonance frequency $f_{\rm hard} = 2.0$ MHz, is not good given its low figure of merit, $R_6 = 1.0$.

This hypothesis is checked in Fig. 6. We see that most of the physical properties of PMMA resonance 2 in Figs. 6(a)–6(c) are similar to the almost-perfect silicon-glass resonance f_A. In one aspect it is even superior: the radiation force in resonance f_2 is not zero at the channel walls $y = \pm\frac{1}{2}W_{\rm fl}$ as is the case with f_A and $f_{\rm hard}$. In this sense f_2 is better to move particles from any starting point in the channel toward the vertical nodal line at $y = 0$. In

TABLE VI. The Q factor, the fluid-domain-averaged acoustic energy density $E_{\rm ac}^{\rm fl}$, the components of the average acoustic radiation force $\bar{\mathbf{F}}^{\rm rad}$, and the figure of merit R for the six pronounced resonances in Fig. 5 in the PMMA device of width $W_{\rm sl} = 3$ mm and height $H_{\rm sl} = 1.175$ mm for $d_0 = 0.3$ nm.

Resonance	Frequency (MHz)	Q	$E_{\rm ac}^{\rm fl}$ (Pa)	$\bar{F}_y^{\rm rad}$ (pN)	$\bar{F}_z^{\rm rad}$ (pN)	R
1	1.0425	141	6.63	5.19	0.78	6.7
2	1.1320	147	4.40	3.91	0.26	14.9
3	1.3815	131	2.14	2.21	0.34	6.6
4	1.4530	136	7.72	8.22	1.34	6.1
5	1.7810	129	7.93	8.36	7.27	1.2
6	1.9045	116	2.32	1.50	1.48	1.0

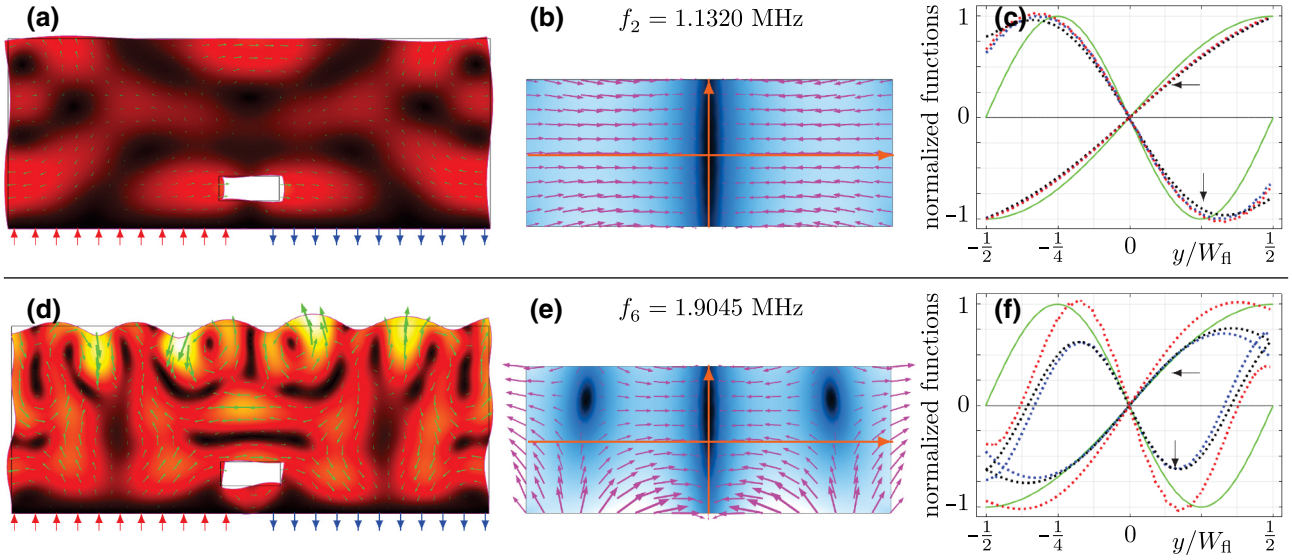

FIG. 6. Numerical results for resonances 2 and 6 in Fig. 5 of the PMMA device. (a)–(c) are for $f_2 = 1.1320$ MHz. (a) Vector plot in the solid domain Ω_{sl} of the displacement field $\mathbf{u}$ (green arrows) and color plot of its amplitude u from 0 nm (black) to 25 nm (light yellow). To be visible, the nanometer-scale displacement has been increased by a factor of 3000. (b) The radiation force $\mathbf{F}^{\mathrm{rad}}$ on a 10-μm-diameter spherical polystyrene tracer particle as a function of its position in the fluid domain Ω_{fl}. Color plot of the magnitude F^{rad} from 0 pN (black) to 9 pN (white) and vector plot (magenta arrows) of $\mathbf{F}^{\mathrm{rad}}$. (c) The normalized pressure p/p_{norm} (half-wave, $p_{\mathrm{norm}} = 150$ kPa) and y component of the radiation force $F_y^{\mathrm{rad}}/F_{\mathrm{norm}}^{\mathrm{rad}}$ (full wave, $F_{\mathrm{norm}}^{\mathrm{rad}} = 5.4$ pN) along the top, center, and bottom horizontal lines at $z = 0.9H_{\mathrm{fl}}$ (blue dots), $z = 0.5H_{\mathrm{fl}}$ (black dots), and $z = 0.1H_{\mathrm{fl}}$ (red dots), respectively. (d),(e),(f) are as (a),(b),(c), respectively, but for $f_6 = 1.9045$ MHz with $p_{\mathrm{norm}} = 135$ kPa and $F_{\mathrm{norm}}^{\mathrm{rad}} = 6.8$ pN.

contrast, the plots in Figs. 6(d)–6(f) show that the acoustic forces in the channel, induced by the whole-system resonance in the PMMA device, result in a radiation force that only in the middle part of the fluid domain points toward the center line. At the edges it points the opposite way. Also a strong vertical component is observed. Clearly in this case the low figure of merit is correctly predicting a resonance not well suited for acoustophoretic applications corresponding to the acoustically hard system.

With this example, we have demonstrated the main point of this paper: microchannels embedded in acoustically soft materials are not able to support a resonance close to the ideal hard-wall resonance. However, whole-system resonances, primarily defined by having a relatively large displacement field in the large solid domain, may nevertheless induce a pressure field in the small fluid domain, and have properties suitable for acoustophoretic applications. We identify these few acoustophoretically useful whole-system ultrasound resonances as those peaks in the spectra of the energy and the radiation-force components that have the largest figure of merit R. These modes are of a quality comparable to that of the BAW modes in conventional systems.

On the basis of these results, we formulate the WSUR principle, according to which good acoustophoresis can be obtained in liquid-filled cavities driven by acoustic resonance modes of the whole system defined by the outer high-contrast solid-air interface and not, as conventionally, by the inner liquid-solid interface of the cavity itself. These WSUR modes may be identified numerically by our maximizing an appropriately defined figure of merit R, such as Eq. (13).

B. The width dependence of the PMMA device

We further demonstrate the use of the above whole-system-ultrasound-resonance principle by studying the width dependency of the resonances in the PMMA device. In Fig. 7 we show a scatter plot of resonances as a function of the device width W_{sl} from 1 to 6 mm and of the actuation frequency f_0 from 1 to 2.1 MHz. The area of each data point is proportional to the magnitude $\bar{F}_y^{\mathrm{rad}}$. The maximal amplitude is $\bar{F}_y^{\mathrm{rad}} = 337$ pN, obtained for $W_{\mathrm{sl}} = 1.3$ mm and $f = 1.328$ MHz, and we have left out resonances with a magnitude lower than $\bar{F}_y^{\mathrm{rad}} = 0.3$ pN. The color code of the points goes from black at $\bar{F}^{\mathrm{rad}} = 0.03$ pN to yellow at $\bar{F}^{\mathrm{rad}} = 30$ pN.

To visualize the figure of merit R of the resonance points in Fig. 7, we add a thick black rim to the resonance points with $R \geq 10$ and a thin black rim to points with $5 \leq R < 10$. The highest figure of merit is 27.3, obtained for $W_{\mathrm{sl}} = 3.5$ mm and $f = 1.054$ MHz. Using such a plot, we are able to efficiently map out the parameter space in the hunt for suitable device designs to make all-polymer devices able to produce good acoustophoresis.

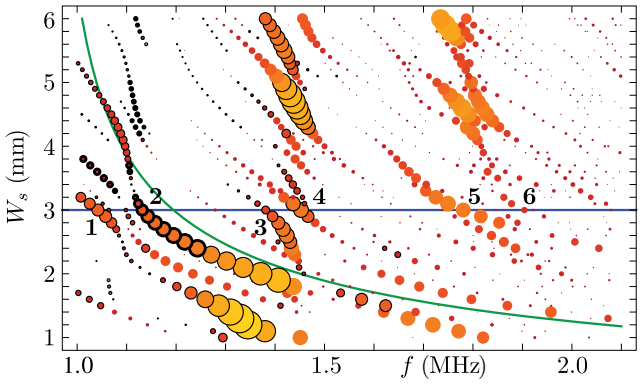

FIG. 7. The average radiation force component $\bar{F}_y^{\mathrm{rad}}$ in the fluid domain in a PMMA device at resonance for a 10-μm-diameter polystyrene tracer particle plotted as a colored scatter plot from 0.03 pN (black) to 30 pN (yellow) versus the polymer chip width W_{sl} and the actuation frequency f . The area of each data point is proportional to the magnitude of $\bar{F}_y^{\mathrm{rad}}$. Resonances with a figure of merit $5 \le R < 10$ and $10 \le R$ are further marked with a thin black rim and a thick black rim, respectively. The horizontal blue line and resonances 1–6 correspond to the line plot in Fig. 5. The green curve is the simplified analytical prediction $W_{\mathrm{sl}}^{(1/2,1)}$, Eq. (15).

It is clear from Fig. 7 that the acoustophoretically good resonance 2 lies on a curve of resonance points for which the resonance frequency increases as the device width W_{sl} decreases. To understand this behavior, we study more closely the displacement field of resonance 2 in Fig. 6(a). We note that not only is there half a shear wave along the y axis due to the actuation but there is also a full shear wave along the z axis. We denote this resonance as the $(\frac{1}{2},1)$ resonance. In a simplistic model of shear-wave propagation of velocity c_{tr} decoupled from the longitudinal wave, we predict the resonance frequency $f_{(1/2,1)}$ for the $(\frac{1}{2},1)$ resonance to be

$$f_{(1/2,1)} = c_{\mathrm{tr}}\sqrt{\frac{2^2}{W_{\mathrm{sl}}^2}+\frac{1^2}{H_{\mathrm{sl}}^2}} \quad \text{or} \quad W_{\mathrm{sl}}^{(1/2,1)}(f) = \frac{2}{\sqrt{\frac{f^2}{c_{\mathrm{tr}}^2}-\frac{1}{H_{\mathrm{sl}}^2}}}. \tag{15}$$

As seen from Fig. 7 (green curve), this naïve prediction is in fair agreement with the line of resonance points to which resonance 2 belongs. At the position of the fluid domain, this particular shear wave results in a horizontal oscillating displacement field that is compatible with the ideal standing pressure half-wave in the channel.

VI. RESULTS FOR THE 3D MODEL OF AN ALL-POLYMER PMMA DEVICE

A more-realistic test of the whole-system-resonance principle for a device in three dimensions is shown in Fig. 8 for a microchannel of length $L_{\mathrm{fl}} = 40$ mm embedded in a PMMA chip of length $L_{\mathrm{sl}} = 50$ mm and with the same 2D cross section as above; see Table V. The ultrasound actuation of amplitude $d_0 = 0.3$ nm is antisymmetric in the y direction and independent of x along the entire bottom as sketched in Fig. 2(b). The whole-system-resonance principle is now used to identify resonances useful for acoustophoresis in this coupled polymer-water system. The frequency-dependent volume-averaged acoustic radiation force $\bar{F}_y^{\mathrm{rad}}$ is shown in Fig. 8(d), and it reveals two strong resonances α and β at $f_\alpha = 1.455$ MHz and $f_\beta = 1.785$ MHz with properties listed in Table VII. Their respective figures of merit (13), $R_\alpha = 32.5$ and $R_\beta = 1.7$,

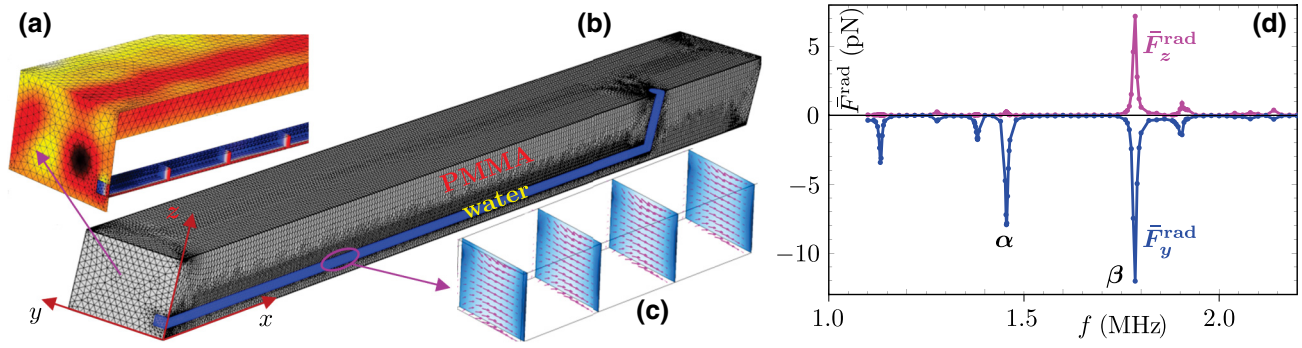

FIG. 8. Numerical simulation of a water-filled microchannel of length $L_{\mathrm{fl}} = 40$ mm, width $W_{\mathrm{fl}} = 375$ μm, and height $H_{\mathrm{fl}} = 150$ μm embedded in a PMMA chip of length $L_{\mathrm{sl}} = 50$ mm, width $W_{\mathrm{sl}} = 3$ mm, and height $H_{\mathrm{sl}} = 1175$ μm, and actuated at the resonance frequency $f = 1.455$ MHz. Because of the symmetry at the yz and xz planes, only the quarter domain $0 < x < \frac{1}{2}L_{\mathrm{sl}}$ and $0 < y < \frac{1}{2}W_{\mathrm{sl}}$ is simulated as in Ref. [59]. The antisymmetric actuation in Fig. 2(b) is used with amplitude $d_0 = 0.3$ nm. (a) Color plots of the amplitude of the displacement u from 0 nm (black) to 4.5 nm (white) on the outer PMMA surface and the pressure p from 0 kPa (red) to 190 kPa (blue) near the symmetry plane $x = 0$ of the system. (b) The finite-element mesh (thin gray lines) used in the simulation. (c) The radiation force $\mathbf{F}^{\mathrm{rad}}$ on 10-μm-diameter polystyrene tracer particles, as in Fig. 6(b), in a short section of the microchannel. (d) The frequency dependency of the components of the volume-averaged acoustic radiation force $\bar{F}_y^{\mathrm{rad}}$ and $\bar{F}_z^{\mathrm{rad}}$ showing two pronounced resonances α and β at $f_\alpha = 1.455$ MHz and $f_\beta = 1.785$ MHz.

TABLE VII. The Q factor, the fluid-domain-averaged acoustic energy density E_{ac}^{fl}, the components of the average acoustic radiation force $\bar{\mathbf{F}}^{rad}$, and the figure of merit R for resonances α and β in Fig. 8(d) in the 3D PMMA device of length $L_{sl} = 50$ mm, width $W_{sl} = 3$ mm, and height $H_{sl} = 1.175$ mm for antisymmetric actuation of amplitude $d_0 = 0.3$ nm.

Resonance	Frequency (MHz)	Q	E_{ac}^{fl} (Pa)	$\bar{F}_y^{rad}$ (pN)	$\bar{F}_z^{rad}$ (pN)	R
α	1.455	162	4.00	7.94	0.24	32.5
β	1.785	172	6.33	12.06	7.18	1.7

indicate that resonance α is more likely to have good properties for acoustophoresis. This is verified by the detailed structure of the pressure field in Fig. 8(a) and the acoustic radiation force $\mathbf{F}^{rad}$ represented by four vertical cut-planes in Fig. 8(c). The acoustic energy density at resonance α is predicted to be $E_{ac}^{fl} = 4.0$ Pa for the assumed actuation amplitude $d_0 = 0.3$ nm.

Preliminary experiments performed by Pelle Ohlson and Ola Jakobsson at AcouSort AB in Lund, Sweden, on PMMA devices nominally identical to the one simulated here have confirmed the existence of a whole-system ultrasound resonance at $f = 1.55$ MHz with an acoustic energy density of $E_{ac}^{fl} = 12$ Pa fully capable of obtaining acoustophoretic focusing on suspended 10-μm-diameter polystyrene tracer particles[63]. The predicted whole-system resonance frequency $f_\alpha = 1.455$ MHz is only 6% lower than the observed frequency but is 27% lower than the hard-wall resonance, and the predicted acoustic energy density $E_{ac} = 4$ Pa will equal the observed acoustic energy density if the assumed actuation amplitude d_0 is increased by a factor of $\sqrt{12\ \text{Pa}/4\ \text{Pa}} = 1.7$ from 0.3 to 0.5 nm. A detailed report of these experiments and their comparison with simulations will be given elsewhere.

VII. CONCLUDING DISCUSSION

We present a numerical study of an acoustically soft device consisting of a fluid channel inside a PMMA chip, where a single split or two separate ultrasound transducers operate in antiphase to excite a standing ultrasound wave in the entire polymer chip. The model takes into account the fully coupled longitudinal and transverse displacement waves in the solid domain and their coupling with the pressure field in the fluid domain.

The nearly identical specific acoustic impedances for PMMA (and other polymers, see Fig. 9) and water does not allow localized resonances in the water domain that are decoupled from the solid domain, as is usually the case in acoustically hard systems such as the conventional silicon-glass devices. Thus for all-polymer systems, the conventional thinking in terms of standing half-wave resonances in the fluid domain cannot be maintained. Instead, the acoustic fields in the two domains are strongly coupled, and given its large volume compared with that of the fluid domain, the solid domain largely determines the resonance behavior. Nevertheless, we find WSURs that support good acoustophoretic action in the water channel. These WSURs can be identified theoretically by our computing resonance peaks in the area-averaged (in two dimensions) or volume-averaged (in three dimensions) acoustophoretic force component $\bar{F}_y^{rad}$ by Eq. (11) in combination with the figure of merit R defined in Eq. (13). We demonstrate in 2D and 3D models how such WSURs have acoustic properties that are comparable to those found in conventional systems used for acoustophoresis.

In the analysis presented here, we focus on acoustophoresis similar to the that obtained by the simple standing pressure half-wave resonance that focuses suspended particles in the vertical center plane in a PMMA device. However, our method is not restricted to this particular type of resonance. It is straightforward to extend it to searching for whole-system resonances with other spatial structures simply by changing the figure of merit to one that reflects the desired type of resonance. Examples of a higher resonance in PMMA and a lower resonance in the rubber PDMS are shown in Fig. 9.

The higher-frequency and more-complex structured resonance in the PMMA device at $f_7 = 2.987$ MHz, shown in Figs. 9(a)–9(c), is located by our changing the figure of merit [Eq. (13)] to the product $\bar{F}_y^{rad}\bar{F}_z^{rad}/(1\ \text{pN}^2)$ to allow large radiation force components both horizontally and vertically. The resonance is reminiscent of a standing half-wave in both the horizontal direction and the vertical direction. With its Q factor of 109 and an acoustic radiation force of magnitude $F^{rad} = 1.9$ pN, this resonance would be fully capable of sustaining good acoustophoresis tending to focus suspended particles in both directions toward the center point of the channel cross section.

To demonstrate the use of the WSUR principle for polymers other than PMMA, we briefly discuss the rubber PDMS, which is often used as a stamp resin in the procedure of soft lithography in the fabrication of microfluidic chips. However, because of the very low transverse sound speed (65 m/s) in PDMS compared with the longitudinal sound speed (1008 m/s), we cannot model the damping with a single damping coefficient Γ_{sl} as in Eq. (1a). Instead, we used complex-valued elastic moduli and set $\Gamma_{sl} = 0$. We use the measured frequency-dependent values of PDMS RTV 615 given for longitudinal waves [64] and transverse waves [65], which at the selected resonance frequency $f = 0.726$ MHz are $C_{11} = (1.035 - i\,0.0026)$ GPa, $C_{44} = (4.31 - i\,0.68)$ MPa, and $C_{12} = (1.027 - i\,0.0012)$ GPa. Using this slightly modified model and the original figure of merit [Eq. (13)], we easily locate the half-wave-like resonance shown in Fig. 9(d) at a frequency $f = 0.726$ MHz nearly 3 times lower than the ideal hard-wall half-wave frequency $f_{hard} =$

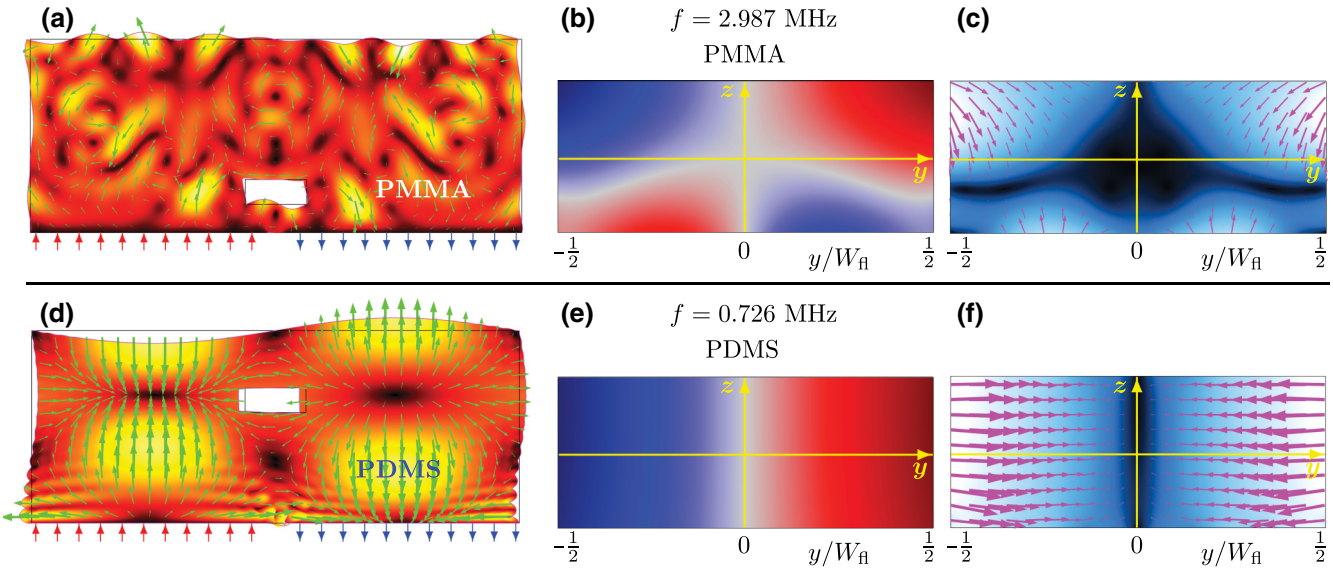

FIG. 9. Numerical results for the PMMA device [(a)–(c)] and a corresponding PDMS device with its cavity displaced 0.5 mm upward [(d)–(e)]. (a) The displacement field **u** (green arrows) and its magnitude (color plot) from 0 nm (black) to 10 nm (white) in the PMMA device as in Fig. 6 but for the higher resonance $f_7 = 2.987$ MHz of $Q = 109$. To be visible, the nanometer-scale displacement has been increased by a factor of 5000. (b) Color plot of the corresponding pressure field p_1 in the water from −210 kPa (blue) to 210 kPa (red). (c) The corresponding radiation force $\mathbf{F}^{\mathrm{rad}}$ (magenta arrows) on a 10-μm-diameter spherical polystyrene tracer particle and its magnitude (color plot) from 0 pN (black) to 1.9 pN (light yellow) as a function of its position in the water. (d) As for (a) but for a PDMS device at the low resonance 0.726 MHz of $Q = 122$ and with the displacement magnitude u from 0 nm (black) to 19 nm (light yellow). (e) The pressure field p_1 as in (b) but with higher amplitude 310 kPa. (f) The radiation force $\mathbf{F}^{\mathrm{rad}}$ as in (c) but with lower amplitude 0.3 pN.

1.985 MHz. The effect of the low transverse sound speed is seen as the horizontal ripple waves near the bottom of the device and decaying away form the transducer. To avoid these ripples, the water-filled cavity has been shifted upward by 0.5 mm compared to the PMMA device. The resulting fields in the cavity, shown in Figs. 9(e) and 9(f), are ideal for acoustophoresis with focusing at the vertical center plane. The Q factor of 122 is relatively high, as is comparable to that of conventional devices, and the resulting radiation force has a reasonable magnitude $F^{\mathrm{rad}} = 0.3$ pN. It is remarkable that the high damping of PDMS mainly lies in the transverse wave propagation, and that in the given geometry and actuation scheme it does not play a dominant role.

Preliminary experiments performed at AcouSort AB [63] on the specific PMMA system modeled here in three dimensions verified the existence of WSURs and their ability to generate good acoustophoresis of a quality fully comparable to that obtained in conventional silicon-glass devices. It would, of course, be interesting also to verify our predictions for WSURs in PDMS devices experimentally but this has not yet been done. Moreover, we have initiated a study on recently developed structured multimaterial fibers [66] to test the WSUR principle in more-complex geometries.

On the basis of the examples of its use, we believe that the whole-system-ultrasound-resonance principle presented in this paper has the potential of playing an important role in the development of high-quality, all-polymer acoustofluidic devices using different materials and geometries: it provides physical insight and it can be used in the design process.

ACKNOWLEDGMENTS

R.M. was supported by the People Programme (Marie Curie Actions) of the European Union's Seventh Framework Programme (FP7/2007-2013) under REA Grant Agreement No. 609405 (COFUNDPostdocDTU). We are grateful for the discussions on experimental realization of our ideas that we have had with Pelle Ohlsson, Ola Jakobsson, and Torsten Freltoft from AcouSort AB and with Thomas Laurell at Lund University.

[1] A. Lenshof, C. Magnusson, and T. Laurell, Acoustofluidics 8: Applications in acoustophoresis in continuous flow microsystems, Lab Chip **12**, 1210 (2012).

[2] M. Gedge and M. Hill, Acoustofluidics 17: Surface acoustic wave devices for particle manipulation, Lab Chip **12**, 2998 (2012).

[3] E. K. Sackmann, A. L. Fulton, and D. J. Beebe, The present and future role of microfluidics in biomedical research, Nature **507**, 181 (2014).

[4] T. Laurell and A. Lenshof, eds., *Microscale Acoustofluidics* (Royal Society of Chemistry, Cambridge, 2015).

[5] M. Antfolk and T. Laurell, Continuous flow microfluidic separation and processing of rare cells and bioparticles found in blood - a review, Anal. Chim. Acta **965**, 9 (2017).

[6] P. Thevoz, J. D. Adams, H. Shea, H. Bruus, and H. T. Soh, Acoustophoretic synchronization of mammalian cells in microchannels, Anal. Chem. **82**, 3094 (2010).

[7] P. Augustsson, C. Magnusson, M. Nordin, H. Lilja, and T. Laurell, Microfluidic, label-free enrichment of prostate cancer cells in blood based on acoustophoresis, Anal. Chem. **84**, 7954 (2012).

[8] R. Zmijan, U. S. Jonnalagadda, D. Carugo, Y. Kochi, E. Lemm, G. Packham, M. Hill, and P. Glynne-Jones, High throughput imaging cytometer with acoustic focussing, RSC Adv. **5**, 83206 (2015).

[9] M. Ohlin, I. Iranmanesh, A. E. Christakou, and M. Wiklund, Temperature-controlled MPA-pressure ultrasonic cell manipulation in a microfluidic chip, Lab Chip **15**, 3341 (2015).

[10] D. J. Collins, B. Morahan, J. Garcia-Bustos, C. Doerig, M. Plebanski, and A. Neild, Two-dimensional single-cell patterning with one cell per well driven by surface acoustic waves, Nat. Commun. **6**, 8686 (2015).

[11] F. Guo, Z. Mao, Y. Chen, Z. Xie, J. P. Lata, P. Li, L. Ren, J. Liu, J. Yang, M. Dao, S. Suresh, and T. J. Huang, Three-dimensional manipulation of single cells using surface acoustic waves, PNAS **113**, 1522 (2016).

[12] P. Augustsson, J. T. Karlsen, H.-W. Su, H. Bruus, and J. Voldman, Iso-acoustic focusing of cells for size-insensitive acousto-mechanical phenotyping, Nat. Commun. **7**, 11556 (2016).

[13] P. Ohlsson, M. Evander, K. Petersson, L. Mellhammar, A. Lehmusvuori, U. Karhunen, M. Soikkeli, T. Seppa, E. Tuunainen, A. Spangar, P. von Lode, K. Rantakokko-Jalava, G. Otto, S. Scheding, T. Soukka, S. Wittfooth, and T. Laurell, Integrated acoustic separation, enrichment, and microchip polymerase chain reaction detection of bacteria from blood for rapid sepsis diagnostics, Anal. Chem. **88**, 9403 (2016).

[14] B. Hammarström, B. Nilson, T. Laurell, J. Nilsson, and S. Ekström, Acoustic trapping for bacteria identification in positive blood cultures with MALDI-TOF MS, Anal. Chem. **86**, 10560 (2014).

[15] G. Sitters, D. Kamsma, G. Thalhammer, M. Ritsch-Marte, E. J. G. Peterman, and G. J. L. Wuite, Acoustic force spectroscopy, Nat. Meth. **12**, 47 (2015).

[16] B. W. Drinkwater, Dynamic-field devices for the ultrasonic manipulation of microparticles, Lab Chip **16**, 2360 (2016).

[17] D. J. Collins, C. Devendran, Z. Ma, J. W. Ng, A. Neild, and Y. Ai, Acoustic tweezers via sub-time-of-flight regime surface acoustic waves, Sci. Adv. **2**, e1600089 (2016).

[18] H. G. Lim, Y. Li, M.-Y. Lin, C. Yoon, C. Lee, H. Jung, R. H. Chow, and K. K. Shung, Calibration of trapping force on cell-size objects from ultrahigh-frequency single-beam acoustic tweezer, IEEE T. Ultrason. Ferr. **63**, 1988 (2016).

[19] D. Baresch, J.-L. Thomas, and R. Marchiano, Observation of a Single-beam Gradient Force Acoustical Trap for Elastic Particles: Acoustical Tweezers, Phys. Rev. Lett. **116**, 024301 (2016).

[20] G. P. Gautam, T. Burger, A. Wilcox, M. J. Cumbo, S. W. Graves, and M. E. Piyasena, Simple and inexpensive micromachined aluminum microfluidic devices for acoustic focusing of particles and cells, Anal. Bioanal. Cham. **410**, 3385 (2018).

[21] A. Fornell, K. Cushing, J. Nilsson, and M. Tenje, Binary particle separation in droplet microfluidics using acoustophoresis, Appl. Phys. Lett. **112**, 063701 (2018).

[22] K. Petersson, O. Jakobsson, P. Ohlsson, P. Augustsson, S. Scheding, J. Malm, and T. Laurell, Acoustofluidic hematocrit determination, Anal. Chim. Acta **1000**, 199 (2018).

[23] C. Magnusson, P. Augustsson, A. Lenshof, Y. Ceder, T. Laurell, and H. Lilja, Clinical-scale cell-surface-marker independent acoustic microfluidic enrichment of tumor cells from blood, Anal. Chem. **89**, 11954 (2017).

[24] D. Ahmed, A. Ozcelik, N. Bojanala, N. Nama, A. Upadhyay, Y. Chen, W. Hanna-Rose, and T. J. Huang, Rotational manipulation of single cells and organisms using acoustic waves, Nat. Commun. **7**, 11085 (2016).

[25] W. Zhou, J. Wang, K. Wang, B. Huang, L. Niu, F. Li, F. Cai, Y. Chen, X. Liu, X. Zhang, H. Cheng, L. Kang, L. Meng, and H. Zheng, Ultrasound neuro-modulation chip: Activation of sensory neurons in Caenorhabditis elegans by surface acoustic waves, Lab Chip **17**, 1725 (2017).

[26] P. Sehgal and B. J. Kirby, Separation of 300 and 100 nm particles in Fabry-Perot acoustofluidic resonators, Anal. Chem. **89**, 12192 (2017).

[27] M. Wu, Z. Mao, K. Chen, H. Bachman, Y. Chen, J. Rufo, L. Ren, P. Li, L. Wang, and T. J. Huang, Acoustic separation of nanoparticles in continuous flow, Adv. Funct. Mater. **27**, 1606039 (2017).

[28] D. J. Collins, R. O'Rorke, C. Devendran, Z. Ma, J. Han, A. Neild, and Y. Ai, Self-aligned Acoustofluidic Particle Focusing and Patterning in Microfluidic Channels from Channel-based Acoustic Waveguides, Phys. Rev. Lett. **120**, 074502 (2018).

[29] W. L. Ung, K. Mutafopulos, P. Spink, R. W. Rambach, T. Franke, and D. A. Weitz, Enhanced surface acoustic wave cell sorting by 3D microfluidic-chip design, Lab Chip **17**, 4059 (2017).

[30] K. Park, J. Park, J. H. Jung, H. Ahmed, and H. J. Sung, In-droplet microparticle separation using travelling surface acoustic wave, Biomicrofluidics **11**, 064112 (2017).

[31] B. J. Kim and E. Meng, Review of polymer MEMS micromachining, J. Micromech. Microeng. **26**, 013001 (2016).

[32] N. Harris, M. Hill, A. Keating, and P. Baylac-Choulet, A lateral mode flow-through PMMA ultrasonic separator, Int. J. Appl. Biomed. Eng. **5**, 20 (2012).

[33] A. Mueller, A. Lever, T. V. Nguyen, J. Comolli, and J. Fiering, Continuous acoustic separation in a thermoplastic microchannel, J. Micromech. Microeng. **23**, 125006 (2013).

[34] I. Gonzalez, M. Tijero, A. Martin, V. Acosta, J. Berganzo, A. Castillejo, M. M. Bouali, and J. Luis Soto, Optimizing polymer lab-on-chip platforms for ultrasonic manipulation: Influence of the substrate, Micromachines **6**, 574 (2015).

[35] C. Yang, Z. Li, P. Li, W. Shao, P. Bai, and Y. Cui, Acoustic particle sorting by integrated micromachined ultrasound transducers on polymerbased microchips, IEEE International Ultrasonics Symposium (IUS), 1 (2017).

[36] W. J. Savage, J. R. Burns, and J. Fiering, Safety of acoustic separation in plastic devices for extracorporeal blood processing, Transfusion **57**, 1818 (2017).
[37] R. Silva, P. Dow, R. Dubay, C. Lissandrello, J. Holder, D. Densmore, and J. Fiering, Rapid prototyping and parametric optimization of plastic acoustofluidic devices for blood-bacteria separation, Biomed. Microdevices **19**, 70 (2017).
[38] C. Lissandrello, R. Dubay, K. T. Kotz, and J. Fiering, Purification of lymphocytes by acoustic separation in plastic microchannels, SLAS Technol. **23**, 352 (2018).
[39] P. Augustsson, R. Barnkob, S. T. Wereley, H. Bruus, and T. Laurell, Automated and temperature-controlled micro-PIV measurements enabling long-term-stable microchannel acoustophoresis characterization, LabChip **11**, 4152 (2011).
[40] P. B. Muller, R. Barnkob, M. J. H. Jensen, and H. Bruus, A numerical study of microparticle acoustophoresis driven by acoustic radiation forces and streaming-induced drag forces, Lab Chip **12**, 4617 (2012).
[41] P. B. Muller and H. Bruus, Numerical study of thermoviscous effects in ultrasound-induced acoustic streaming in microchannels, Phys. Rev. E **90**, 043016 (2014).
[42] P. B. Muller and H. Bruus, Theoretical study of time-dependent, ultrasound-induced acoustic streaming in microchannels, Phys. Rev. E **92**, 063018 (2015).
[43] J. S. Bach and H. Bruus, Theory of pressure acoustics with viscous boundary layers and streaming in curved elastic cavities, J. Acoust. Soc. Am. **144**, 766 (2018).
[44] R. Barnkob, P. Augustsson, T. Laurell, and H. Bruus, Measuring the local pressure amplitude in microchannel acoustophoresis, Lab Chip **10**, 563 (2010).
[45] R. Barnkob, P. Augustsson, T. Laurell, and H. Bruus, Acoustic radiation- and streaming-induced microparticle velocities determined by microparticle image velocimetry in an ultrasound symmetry plane, Phys. Rev. E **86**, 056307 (2012).
[46] P. B. Muller, M. Rossi, A. G. Marin, R. Barnkob, P. Augustsson, T. Laurell, C. J. Kähler, and H. Bruus, Ultrasound-induced acoustophoretic motion of microparticles in three dimensions, Phys. Rev. E **88**, 023006 (2013).
[47] H. Sutherland and R. Lingle, Acoustic characterization of polymethyl methacrylate and 3 epoxy formulations, J. Appl. Phys. **43**, 4022 (1972).
[48] H. Sutherland, Acoustical determination of shear relaxation functions for polymethyl methacrylate and Epon 828-Z, J. Appl. Phys. **49**, 3941 (1978).
[49] J. E. Carlson, J. van Deventer, A. Scolan, and C. Carlander, Frequency and temperature dependence of acoustic properties of polymers used in pulse-echo systems, IEEE Ultrasonics Symposium, 885 (2003).
[50] P. H. Mott, J. R. Dorgan, and C. M. Roland, The bulk modulus and Poisson's ratio of "incompressible" materials, J. Sound Vibr. **312**, 572 (2008).
[51] M. Treiber, J.-Y. Kim, L. J. Jacobs, and J. Qu, Correction for partial reflection in ultrasonic attenuation measurements using contact transducers, J. Acoust. Soc. Am. **125**, 2946 (2009).
[52] Glass Silicon Constraint Substrates, CORNING, Houghton Park C-8, Corning, NY 14831, USA, http://www.valleydesign.com/Datasheets/Corning Pyrex 7740.pdf (11 November 2018).
[53] M. A. Hopcroft, W. D. Nix, and T. W. Kenny, What is the Young's modulus of silicon, J. Microelectromech. Syst. **19**, 229 (2010).
[54] S. Kasarova, N. Sultanova, and I. Nikolov, Polymer materials in optical design, Bulg. Chem. Commun. **47**, 44 (2015
[55] P. Hahn and J. Dual, A numerically efficient damping model for acoustic resonances in microfluidic cavities, Phys. Fluids **27**, 062005 (2015).
[56] B. Hartmann and J. Jarzynski, Polymer sound speeds and elastic constants, Naval Ordnance Laboratory Report NOLTR 72-269, 1 (1972), https://apps.dtic.mil/dtic/tr/fulltext/u2/755695.pdf.
[57] J. T. Karlsen and H. Bruus, Forces acting on a small particle in an acoustical field in a thermoviscous fluid, Phys. Rev. E **92**, 043010 (2015).
[58] L. D. Landau and E. M. Lifshitz, *Theory of Elasticity. Course of Theoretical Physics* (Pergamon Press, Oxford, 1986). 3rd ed., Vol. 7.
[59] M. W. H. Ley and H. Bruus, Three-dimensional Numerical Modeling of Acoustic Trapping in Glass Capillaries, Phys. Rev. Applied **8**, 024020 (2017).
[60] J. Dual and T. Schwarz, Acoustofluidics 3: Continuum mechanics for ultrasonic particle manipulation, Lab Chip **12**, 244 (2012).
[61] M. Settnes and H. Bruus, Forces acting on a small particle in an acoustical field in a viscous fluid, Phys. Rev. E **85**, 016327 (2012).
[62] COMSOL Multiphysics 5.3a, www.comsol.com (2017).
[63] AcouSort AB, www.acousort.com (private communication), 2018.
[64] D. Folds, Speed of sound and transmission loss in silicone rubbers at ultrasonic frequencies, J. Acoust. Soc. Am. **56**, 1295 (1974).
[65] E. L. Madsen, Ultrasonic shear wave properties of soft tissues and tissuelike materials, J. Acoust. Soc. Am. **74**, 1346 (1983).
[66] R. Yuan, J. Lee, H.-W. Su, E. Levy, T. Khudiyev, J. Voldman, and Y. Fink, Microfluidics in structured multimaterial fibers, PNAS **115**, E10830 (2018).